Analysis of Water Wave Problems Containing Single and Multiple Cylinders by Using Degenerate Kernel Method

Jeng-Tzong Chen
Department of Harbor and River Engineering and Department of Mechanical and Mechatronic Engineering,
National Taiwan Ocean University Keelung, Taiwan, China

Chien-Feng Wu and Jia-Wei Lee
Department of Harbor and River Engineering, National Taiwan Ocean University
Keelung, Taiwan, China

Yu-Chih Hsiao
Department of Systems Engineering and Naval Architecture, National Taiwan Ocean University
Keelung, Taiwan, China

In this paper, water wave problems containing circular cylinders are solved by employing the null-field boundary integral equation in conjunction with degenerate kernels and the Fourier series. The fundamental solution is expanded to the degenerate kernel in the polar coordinates for problems containing circular boundaries. The boundary densities are expanded by using the natural base of the Fourier series. By this means, the field point can be located exactly on the real boundary free of calculating Cauchy and Hadamard principal values. Since errors attribute from the number of terms of the boundary densities, the present method can be seen as a semi-analytical approach. Both single and multiple cylinders are considered. Regarding the case of a single cylinder, our results are compared with those of the boundary element method (BEM) in the literature. The present method achieves higher accuracy and faster convergence than BEM. The near-trapped mode phenomena are observed. The effect of disorder of circular cylinders is also investigated in this paper. Finally, the free-surface elevation of the water wave containing a circular cylinder is animated by using the Mathematica software.

INTRODUCTION

Understanding the multiple scattering of water waves by arrays of cylinders is a problem of long-standing interest. Water wave problems containing circular cylinders have also attracted the attention of researchers from many countries with long coast lines, such as Taiwan, the USA and Japan. Over the past 40 years, investigators have presented several numerical methods, including the finite difference method, finite element method and boundary element method (BEM), to solve several problems in ocean engineering. In this field, water wave forces are of considerable importance for structures for structural safety, so many researchers have undertaken some related studies in different ways of theoretical, experimental and numerical work. MacCamy and Fuchs (1954) derived the exact solution of the horizontal wave force on a single vertical circular cylinder. The experiment data were tested by Chakrabarti and Tam (1975). Au and Brebbia (1983) employed the BEM to solve the water wave problems containing a circular cylinder. Later, Zhu and Moule (1996) used a various discretization mesh to obtain better results than those of Au and Brebbia (1983). Linton and Evans (1990) studied the interaction of water waves with arrays of vertical circular cylinders by using the multipole expansion approach.

Trapped and near-trapped modes may occur for problems containing infinite and truncated periodical patterns of arrays of cylinders, respectively, as shown in Fig. 1. Fig. 1a shows a trapped mode is associated with the existence of a real eigenvalue of the

governing operator. Fig. 1b shows a near-trapped mode is associated with a singularity of the analytic extension of the governing operator close to the real axis. These physical phenomena appear in many fields, such as engineering mathematics, hydraulic engineering, earthquake engineering, ocean engineering and physics. The trap phenomena are described item by item.

• Engineering mathematics. When a spring system is subjected to an incident wave, the spring may have a near-trapped mode under a certain arrangement of spring constant and distance between 2 springs (Chen et al., 2009a).

• Hydraulic engineering. There exists a stepped ridge and that water is unable to propagate from a shallow area to a deep area (Mei, 1983).

• Earthquake engineering. Here, the surface wave may seriously result in damage for structures. For a thin-layer inclusion in a half-space medium, a trapped wave may occur—for example, the Love wave or the Stonely wave (Graff, 1975).
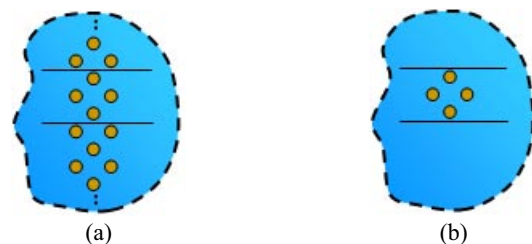

Fig. 1 (a) Trapped mode of an infinite periodical array of cylinders; (b) near-trapped mode of a truncated periodical array of cylinders

• Quantum physics. The trapped mode occurs in physics as well as engineering. The bound state in a square-well potential in quantum mechanics is another case of trapped modes (Postnova and Craster, 2008).

• Ocean engineering (our focus). The construction of an off-shore platform is subjected to wave loads year-round. Duclos and Clément (2004) proposed a simplified model of linear theory to simulate the interaction between cylinders subjected to the incident wave. In this analysis, a specific distance between cylinders in conjunction with a certain wave number may cause trapped and near-trapped modes. This topic is our main concern in this paper.

A near-trapped mode is relative to a scattering frequency. A scattering frequency is a peak of the analytic continuation of the scattering operator. Tabaei and Mei (2009) coined these scattering resonances. Evans and Porter (1999) used the Linton and Evans (1990) method to discover trapping and near-trapping phenomena for the case of bottom-mounted cylinders. Meylan and Taylor (2009) studied the near-trapped mode in the complex plane of water frequency. The near-trapped modes in physics were numerically observed in a consistent way by other works (Evans and Porter, 1999).

Here, we study the near-trapped mode by using the null-field boundary integral equation. This approach has been successfully employed to solve water wave scattering problems across an array of circular cylinders (e.g., Chen et al., 2009b; Wu et al., 2009; Chen et al., 2007a; Chen et al., 2009c). To fully utilize the geometry of the circular boundary, not only the Fourier series for boundary densities but also the degenerate kernels for fundamental solutions are incorporated into the present method. Several advantages over the conventional BEM are achieved, such as mesh-free generation, well-posed model, principal-value free, elimination of boundary-layer effect and exponential convergence.

PROBLEM STATEMENT AND INTEGRAL FORMULATION

Problem Statement

Now we assume N vertical cylinders mounted at $z = -h$ upward to the free surface as shown in Fig. 2. The governing equation of the water wave problem is the Laplace equation:

$$\nabla^2 \Phi(x, y, z, t) = 0, \quad (x, y, z) \in D \tag{1}$$

where D is the domain of interest; ∇^2, the Laplacian operator; $\Phi(x, y, z, t)$, the velocity potential where (x, y) locate in the plane; and z, the vertical direction, which satisfies the boundary conditions of the seabed. The linearized kinematic condition on the bottom is:

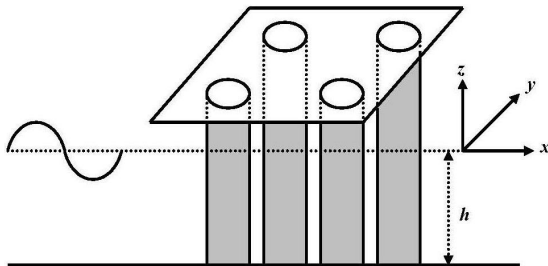$$\left(\frac{\partial \Phi}{\partial z}\right)_{z=-h} = 0 \tag{2}$$

Fig. 2 Problem statement of water waves with array of vertical cylinders

and the linearized condition on the free surface is:

$$\left(-\frac{\omega^2}{g}\Phi + \frac{\partial \Phi}{\partial z}\right)_{z=0} = 0 \tag{3}$$

where g is the acceleration due to gravity. The velocity potential must also satisfy the kinematic conditions on the wetted surface of all bodies:

$$\frac{\partial \Phi}{\partial n} = 0, \quad -h \le z \le 0 \tag{4}$$

where n stands for the normal vector of any body with respect to its local circular coordinate system.

Based on the linearized water wave theory, we can use the technique of separation variables to express the velocity potential in terms of space and time:

$$\Phi(x, y, z, t) = u(x, y)f(z)e^{-i\omega t} \tag{5}$$

where:

$$f(z) = \frac{-igA}{\omega}\frac{\cosh(k(z+h))}{\cosh(kh)} \tag{6}$$

in which h is the water depth, k represents the wave number, ω is the angular frequency, and A denotes the amplitude of the incident wave.

In addition, k and ω satisfy the dispersion relationship as follows:

$$k\tanh(kh) = \frac{\omega^2}{g}. \tag{7}$$

The free-surface elevation of $H(x, y, t)$ can be defined by:

$$H(x, y, t) = \eta(x, y)e^{-i\omega t} \tag{8}$$

where:

$$\eta(x, y) = Au(x, y) \tag{9}$$

The incident plane wave potential is:

$$u_I(x, y) = e^{ik(x\cos\theta_{inc} + y\sin\theta_{inc})} \equiv e^{ikr\cos(\theta - \theta_{inc})} \tag{10}$$

where θ_{inc} is the incident angle.

Substituting Eq. 5 into Eq. 1, we can simplify to the Helmholtz equation:

$$(\nabla^2 + k^2)u(x, y) = 0, \quad (x, y) \in D. \tag{11}$$

Rigid cylinders yield the Neumann boundary condition:

$$\frac{\partial u(x, y)}{\partial n} = 0, \quad (x, y) \in B \tag{12}$$

where B is the boundary of cylinders.

The dynamic pressure can be obtained by:

$$p = -\rho_f \frac{\partial \Phi}{\partial t} = \rho_f gA \frac{\cosh(k(z+h))}{\cosh(kh)}u(x, y)e^{-i\omega t} \tag{13}$$

where ρ_f is the density of fluid. The 2 components of the force X^j on the jth cylinder are given by integrating the pressure over

the circular boundary:

$$\{X^j\} = -\frac{\rho_f g A a_j}{k} \cdot \tanh(kh) \cdot \int_0^{2\pi} u(x,y) \begin{Bmatrix} \cos\theta_j \\ \sin\theta_j \end{Bmatrix} d\theta_j \qquad (14)$$

where a_j denotes the radius of the jth cylinder.

Dual Boundary Integral Equations: Conventional Version

The integral equation for the domain point can be derived from Green's third identity (Chen et al., 2009b):

$$2\pi u(\mathbf{x}) = \int_B T(\mathbf{s},\mathbf{x})u(\mathbf{s})\,dB(\mathbf{s})$$
$$- \int_B U(\mathbf{s},\mathbf{x})t(\mathbf{s})\,dB(\mathbf{s}), \quad \mathbf{x} \in D, \qquad (15)$$

$$2\pi t(\mathbf{x}) = \int_B M(\mathbf{s},\mathbf{x})u(\mathbf{s})\,dB(\mathbf{s})$$
$$- \int_B L(\mathbf{s},\mathbf{x})t(\mathbf{s})\,dB(\mathbf{s}), \quad \mathbf{x} \in D \qquad (16)$$

where s and x are the source and field points, respectively, and $t(\mathbf{s}) = \partial u(\mathbf{s})/\partial \mathbf{n}_s$ and $\mathbf{n}_s$ denote the unit outward normal vectors at source point s. Eqs. 15 and 16 are dual BIEM formulations. However, Eqs. 2~12 are some equations of the mathematical model. Instead of using the PDE of Eq. 11, we solve the problem by using integral equations of Eqs. 15 and 16. The kernel function, $U(\mathbf{s},\mathbf{x}) = -(\pi i/2)H_0^{(1)}(kr)$, is the fundamental solution which satisfies:

$$\nabla^2 U(\mathbf{s},\mathbf{x}) + k^2 U(\mathbf{s},\mathbf{x}) = 2\pi\delta(\mathbf{x}-\mathbf{s}) \qquad (17)$$

where $\delta(\mathbf{x}-\mathbf{s})$ denotes the Dirac-delta function; $H_n^{(1)}(kr) = J_n(kr) + iY_n(kr)$ is the n-th order Hankel function of the first kind; J_n, the n-th order Bessel function of the first kind; Y_n, the n-th order Bessel function of the second kind; $r = |\mathbf{x}-\mathbf{s}|$ and $i^2 = -1$. The other kernel functions, $T(\mathbf{s},\mathbf{x})$, $L(\mathbf{s},\mathbf{x})$, and $M(\mathbf{s},\mathbf{x})$, are defined by:

$$T(\mathbf{s},\mathbf{x}) = \frac{\partial U(\mathbf{s},\mathbf{x})}{\partial \mathbf{n}_s}, \qquad (18)$$

$$L(\mathbf{s},\mathbf{x}) = \frac{\partial U(\mathbf{s},\mathbf{x})}{\partial \mathbf{n}_x}, \qquad (19)$$

$$M(\mathbf{s},\mathbf{x}) = \frac{\partial^2 U(\mathbf{s},\mathbf{x})}{\partial \mathbf{n}_s \partial \mathbf{n}_x} \qquad (20)$$

where $\mathbf{n}_x$ denote the unit outward normal vectors at the field point x.

By moving the field point to the boundary, Eqs. 15 and 16 reduce to:

$$\pi u(\mathbf{x}) = C.P.V. \int_B T(\mathbf{s},\mathbf{x})u(\mathbf{s})\,dB(\mathbf{s})$$
$$- R.P.V. \int_B U(\mathbf{s},\mathbf{x})t(\mathbf{s})\,dB(\mathbf{s}), \quad \mathbf{x} \in B, \qquad (21)$$

$$\pi t(\mathbf{x}) = H.P.V. \int_B M(\mathbf{s},\mathbf{x})u(\mathbf{s})\,dB(\mathbf{s})$$
$$- C.P.V. \int_B L(\mathbf{s},\mathbf{x})t(\mathbf{s})\,dB(\mathbf{s}), \quad \mathbf{x} \in B \qquad (22)$$

where $R.P.V.$, $C.P.V.$ and $H.P.V.$ denote the Riemann principal value (Riemann sum), Cauchy principal value and Hadamard principal value (or Hadamard finite part), respectively. Once the

field point x locates outside the domain ($\mathbf{x} \in D^c$), we obtain the dual null-field integral equations:

$$0 = \int_B T(\mathbf{s},\mathbf{x})u(\mathbf{s})\,dB(\mathbf{s}) - \int_B U(\mathbf{s},\mathbf{x})t(\mathbf{s})\,dB(\mathbf{s}), \quad \mathbf{x} \in D^c, \qquad (23)$$

$$0 = \int_B M(\mathbf{s},\mathbf{x})u(\mathbf{s})\,dB(\mathbf{s}) - \int_B L(\mathbf{s},\mathbf{x})t(\mathbf{s})\,dB(\mathbf{s}), \quad \mathbf{x} \in D^c \qquad (24)$$

where D^c is the complementary domain. Eqs. 15, 16, 23 and 24 are conventional formulations where the point can not be located on the real boundary. Singularity occurs and the concept of principal values is required once Eqs. 21 and 22 are considered. The flux $t(s)$ is the directional derivative of $u(s)$ along the outer normal direction at s. For the interior point, $t(x)$ is artificially defined. For example, $t(\mathbf{x}) = \partial u(\mathbf{s})/\partial x_1$, if $\mathbf{n}_x = (1,0)$ and $t(\mathbf{x}) = \partial u(\mathbf{x})/\partial x_2$, if $\mathbf{n}_x = (0,1)$ where (x_1, x_2) is the coordinate of the field point x.

Dual Boundary Integral Equations: Present Version

Based on the dual boundary integral formulation of the domain point, we have:

$$2\pi u(\mathbf{x}) = \int_B T(\mathbf{s},\mathbf{x})u(\mathbf{s})\,dB(\mathbf{s})$$
$$- \int_B U(\mathbf{s},\mathbf{x})t(\mathbf{s})\,dB(\mathbf{s}), \quad \mathbf{x} \in D \cup B, \qquad (25)$$

$$2\pi t(\mathbf{x}) = \int_B M(\mathbf{s},\mathbf{x})u(\mathbf{s})\,dB(\mathbf{s})$$
$$- \int_B L(\mathbf{s},\mathbf{x})t(\mathbf{s})\,dB(\mathbf{s}), \quad \mathbf{x} \in D \cup B. \qquad (26)$$

Eqs. 25 and 26 are not the same as the conventional formulation since they are valid not only for the points in the domain D but also for the boundary points if the kernels are properly expressed as the interior degenerate kernels. The set of $\mathbf{x}$ in Eqs. 25 and 26 is closed since $\mathbf{x} \in D \cup B$. The flux $t(\mathbf{s})$ is the directional derivative of $u(\mathbf{s})$ along the outer normal direction at $\mathbf{s}$. Eqs. 25 and 26 are termed singular and hypersingular boundary integral equations (BIE), respectively.

Null-Field Integral Formulation in Conjunction with Degenerate Kernel and Fourier Series

By collocating $\mathbf{x}$ outside the domain ($\mathbf{x} \in D^c$, complementary domain), we obtain the null-field integral equations:

$$0 = \int_B T(\mathbf{s},\mathbf{x})u(\mathbf{s})\,dB(\mathbf{s})$$
$$- \int_B U(\mathbf{s},\mathbf{x})t(\mathbf{s})\,dB(\mathbf{s}), \quad \mathbf{x} \in D^c \cup B, \qquad (27)$$

$$0 = \int_B M(\mathbf{s},\mathbf{x})u(\mathbf{s})\,dB(\mathbf{s})$$
$$- \int_B L(\mathbf{s},\mathbf{x})t(\mathbf{s})\,dB(\mathbf{s}), \quad \mathbf{x} \in D^c \cup B. \qquad (28)$$

The collocation point $\mathbf{x}$ can locate on the outside of the domain as well as B if kernels are substituted into proper exterior degenerate kernels. A closed-form fundamental solution can be described by different expressions of degenerate kernels for interior and exterior cases; the BIE for the domain point of Eqs. 25 and 26 and null-field BIE of Eqs. 27 and 28 can include the boundary point. In the real implementation, the null-field point can be located on the real boundary; the degenerate kernel is employed to describe the closed-form fundamental solution in each side. The above-mentioned 4 kernels U, T, L and M are not the same, but have to expand to 2 kinds as shown in Eqs. 29~32. By using the polar coordinates, we can express $\mathbf{x} = (\rho, \phi)$ and $\mathbf{s} = (R, \theta)$. In view

of the degenerate kernels, the 4 kernels U, T, L and M can be expressed in terms of the degenerate kernel as shown here:

$$
\begin{cases}
U^I(\mathbf{s}, \mathbf{x}) = \dfrac{-\pi i}{2} \displaystyle\sum_{m=0}^{M} \varepsilon_m J_m(k\rho) H_m^{(1)}(kR) \cos(m(\theta - \phi)), \\
\qquad R \geq \rho, \\
U^E(\mathbf{s}, \mathbf{x}) = \dfrac{-\pi i}{2} \displaystyle\sum_{m=0}^{M} \varepsilon_m H_m^{(1)}(k\rho) J_m(kR) \cos(m(\theta - \phi)), \\
\qquad R < \rho,
\end{cases}
\tag{29}
$$

$$
\begin{cases}
T^I(\mathbf{s}, \mathbf{x}) = \dfrac{-\pi k i}{2} \displaystyle\sum_{m=0}^{M} \varepsilon_m J_m(k\rho) H_m'^{(1)}(kR) \cos(m(\theta - \phi)), \\
\qquad R > \rho, \\
T^E(\mathbf{s}, \mathbf{x}) = \dfrac{-\pi k i}{2} \displaystyle\sum_{m=0}^{M} \varepsilon_m H_m^{(1)}(k\rho) J_m'(kR) \cos(m(\theta - \phi)), \\
\qquad R < \rho,
\end{cases}
\tag{30}
$$

$$
\begin{cases}
L^I(\mathbf{s}, \mathbf{x}) = \dfrac{-\pi k i}{2} \displaystyle\sum_{m=0}^{M} \varepsilon_m J_m'(k\rho) H_m^{(1)}(kR) \cos(m(\theta - \phi)), \\
\qquad R > \rho, \\
L^E(\mathbf{s}, \mathbf{x}) = \dfrac{-\pi k i}{2} \displaystyle\sum_{m=0}^{M} \varepsilon_m H_m'^{(1)}(k\rho) J_m(kR) \cos(m(\theta - \phi)), \\
\qquad R < \rho,
\end{cases}
\tag{31}
$$

$$
\begin{cases}
M^I(\mathbf{s}, \mathbf{x}) = \dfrac{-\pi k^2 i}{2} \displaystyle\sum_{m=0}^{M} \varepsilon_m J_m'(k\rho) H_m'^{(1)}(kR) \cos(m(\theta - \phi)), \\
\qquad R \geq \rho, \\
M^E(\mathbf{s}, \mathbf{x}) = \dfrac{-\pi k^2 i}{2} \displaystyle\sum_{m=0}^{M} \varepsilon_m H_m'^{(1)}(k\rho) J_m'(kR) \cos(m(\theta - \phi)), \\
\qquad R < \rho
\end{cases}
\tag{32}
$$

where ε_m is the Neumann factor:

$$
\varepsilon_m =
\begin{cases}
1, & m = 0, \\
2, & m = 1, 2, \ldots, \infty.
\end{cases}
\tag{33}
$$

Eqs. 29~32 are called degenerate kernels (or separable kernels) which can be expanded to finite (M) sums of products of functions of the field point $\mathbf{x}$ alone and functions of the source point $\mathbf{s}$ alone. If we consider the finite sum of series, the kernel is finite rank. Mathematically speaking, the theory of boundary integral equations with the degenerate kernel is nothing but linear algebra. Since the potentials that resulted from $T(\mathbf{s}, \mathbf{x})$ and $L(\mathbf{s}, \mathbf{x})$ are discontinuous across the boundary, the potentials are different when $T(\mathbf{s}, \mathbf{x})$ and $L(\mathbf{s}, \mathbf{x})$ for $R \to \rho^+$ and $R \to \rho^-$. This is why the degenerate kernels of $T(\mathbf{s}, \mathbf{x})$ and $L(\mathbf{s}, \mathbf{x})$ do not include $R = \rho$ in the expression. The degenerate kernels simply serve as the means with which to evaluate regular integrals analytically and take the limits analytically. The reason is that Eqs. 25 and 27 yield the same algebraic equation when the limit is taken from the inside or from the outside of the region. Both limits represent the same algebraic equation, that is, an approximate counterpart of the boundary integral equation, which in the case of a smooth boundary has term $\pi u(\mathbf{x})$ or $\pi t(\mathbf{x})$ on the left-hand side rather than $2\pi u(\mathbf{x})$ or $2\pi t(\mathbf{x})$ for the domain point, or 0 for the point outside the domain. Further, the limiting case to the boundary is also addressed. The Wronskian property of Bessel function

J_m and Y_m can capture continuous and jump behavior across the boundary:

$$
W(J_m(kR), Y_m(kR)) = Y_m'(kR) J_m(kR) - Y_m(kR) J_m'(kR)
$$
$$
= \frac{2}{\pi k R}
\tag{34}
$$

as:

$$
\int_0^{2\pi} (T^I(\mathbf{s}, \mathbf{x}) - T^E(\mathbf{s}, \mathbf{x})) \cos(m\theta) R \, d\theta
$$
$$
= 2\pi \cos(m\phi), \quad \mathbf{x} \in B,
\tag{35}
$$
$$
\int_0^{2\pi} (T^I(\mathbf{s}, \mathbf{x}) - T^E(\mathbf{s}, \mathbf{x})) \sin(m\theta) R \, d\theta
$$
$$
= 2\pi \sin(m\phi), \quad \mathbf{x} \in B.
\tag{36}
$$

After employing Eqs. 35 and 36, Eqs. 25 and 27 yield the same linear algebraic equation when $\mathbf{x}$ is located exactly on the boundary from the domain or the complementing domain. A proof for the Laplace and Helmholtz cases can be found in Chen et al. (2006) and Chen et al. (2007b), respectively.

In order to fully utilize the geometry of the circular boundary, the boundary potential $u(\mathbf{s})$ and its normal flux $t(\mathbf{s})$ can be simulated by using the Fourier series. Thus, we obtain:

$$
u(\mathbf{s}) = a_0 + \sum_{n=1}^{M} (a_n \cos n\theta + b_n \sin n\theta),
\tag{37}
$$
$$
t(\mathbf{s}) = p_0 + \sum_{n=1}^{M} (p_n \cos n\theta + q_n \sin n\theta)
\tag{38}
$$

where a_0, a_n, b_n, p_0, p_n and q_n are the Fourier coefficients and θ is the polar angle. Eqs. 27 and 28 can be easily calculated by employing the orthogonal property of the Fourier series. In the real computation, only the finite $2M + 1$ terms are used in the summation of Eqs. 37 and 38.

Adaptive Observer System

The boundary integral equations are frame indifferent, so the rule of objectivity is obeyed. The adaptive observer system is chosen to fully employ the property of degenerate kernels. Fig. 3 shows the boundary integration for the circular boundaries. It is worth noting that the origin of the observer system can be adaptively located on the center of the corresponding circle under integration to fully utilize the circular boundary's geometry. The dummy variable in the integration on the circular boundary is just the angle (θ) instead of the radial coordinate (R). By using the adaptive system, all the boundary integrals can be determined analytically free of principal value.
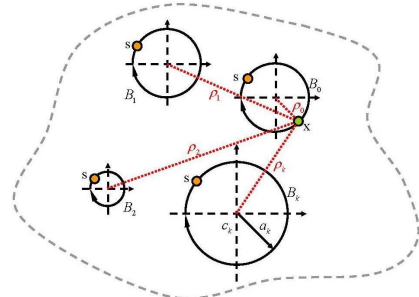

Fig. 3 Adaptive observer system

Linear Algebraic Equation

In order to calculate the $2M + 1$ unknown Fourier coefficients, $2M + 1$ boundary points on each circular boundary need to be collocated. By collocating the null-field point exactly on the kth circular boundary for Eqs. 27 and 28 as shown in Fig. 3, we have:

$$0 = \sum_{j=1}^{N} \int_{B_j} T(\mathbf{s}, \mathbf{x}_k) u(\mathbf{s})\, dB(\mathbf{s})$$
$$- \sum_{j=1}^{N} \int_{B_j} U(\mathbf{s}, \mathbf{x}_k) t(\mathbf{s})\, dB(\mathbf{s}), \quad \mathbf{x}_k \in D^c \cup B, \tag{39}$$

$$0 = \sum_{j=1}^{N} \int_{B_j} M(\mathbf{s}, \mathbf{x}_k) u(\mathbf{s})\, dB(\mathbf{s})$$
$$- \sum_{j=1}^{N} \int_{B_j} L(\mathbf{s}, \mathbf{x}_k) t(\mathbf{s})\, dB(\mathbf{s}), \quad \mathbf{x}_k \in D^c \cup B \tag{40}$$

where N is the number of circular cylinders. Note that the path is anticlockwise for the outer circle; otherwise, it is clockwise. For the B_j integral of the circular boundary, the kernels of $U(\mathbf{s}, \mathbf{x})$, $T(\mathbf{s}, \mathbf{x})$, $L(\mathbf{s}, \mathbf{x})$ and $M(\mathbf{s}, \mathbf{x})$ are respectively expressed in terms of degenerate kernels of Eqs. 29 and 30 with respect to the observer origin at the center of B_j. The boundary densities of $u(\mathbf{s})$ and $t(\mathbf{s})$ are substituted by using the Fourier series of Eqs. 37 and 38, respectively. In the B_j integration, we set the origin of the observer system to collocate at the center c_j of B_j to fully utilize the degenerate kernel and Fourier series. By locating the null-field point on the real boundary B_k from outside the domain D^c in numerical implementation, a linear algebraic system is obtained:

$$[\mathbf{U}]\{\mathbf{t}\} = [\mathbf{T}]\{\mathbf{u}\} \tag{41}$$

$$[\mathbf{L}]\{\mathbf{t}\} = [\mathbf{M}]\{\mathbf{u}\}. \tag{42}$$

For more details on how to derive the influence matrix of U, T, L and M, readers can consult Chen et al., 2009b.

ILLUSTRATIVE EXAMPLES

Case 1: Water Wave Impinging on Circular Cylinder

In this case, we consider the water wave problem by a bottom-mounted vertical rigid circular cylinder. MacCamy and Fuchs (1954) studied this problem, and the exact solution of the horizontal force on the cylinder is:

$$F_x = \frac{4\rho_f g A \tanh kh}{k^2 H_1^{\prime(1)}(ka)}. \tag{43}$$

The force is also obtained by using our degenerate-kernel method:

$$F_x = -\rho_f g A a \frac{1}{k} \tanh kh \left\{ 2\pi i J_1(ka) - \pi^2 ka H_1^{(1)}(ka) J_1'(ka) \right.$$
$$\left. \cdot \left[\left(J_1(ka) - \frac{H_1^{(1)}(ka) J_1'(ka)}{H_1^{\prime(1)}(ka)} \right) \right] \right\}. \tag{44}$$

Although the formulae for the force derived by using our approach look quite different (and awkward) from the literature in Eq. 43, it can be proved to be equivalent by using the Wronskian property of Bessel functions. Numerical results also support this point.
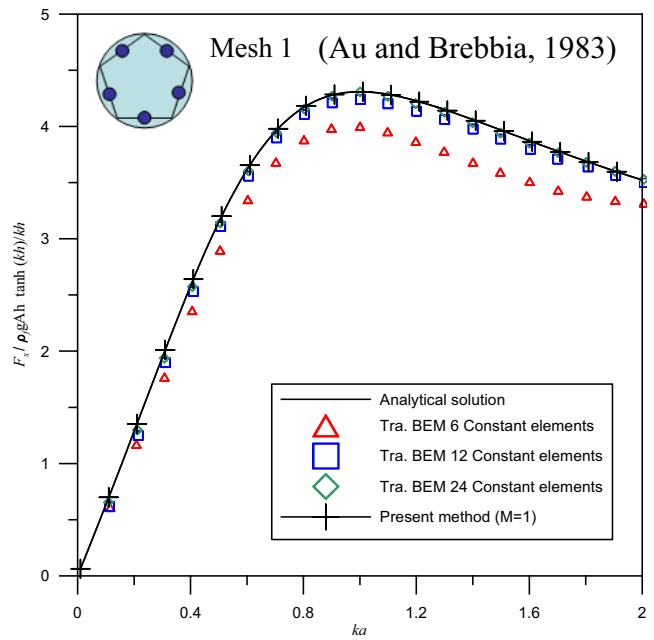

Fig. 4 Horizontal force on single cylinder using Mesh 1 of BEM and null-field BIEM

This problem has also been studied by Au and Brebbia (1983) and Zhu and Moule (1996) by using the BEM of different discretization (Meshes 1 and 2) to match boundary geometry, as shown in Figs. 4 and 5. These results are compared with the present method as shown in Figs. 4 and 5. The nondimensional total horizontal force, $F_X / \{\rho_f g A h \tanh(kh)/kh\}$, is plotted versus ka. Good agreement is reached. The accuracy of the present method is better than that of BEM.

The phase of horizontal force is also plotted and compared with that of BEM (Au and Brebbia, 1983; Zhu and Moule, 1996) and the analytical solution as shown in Fig. 6. A good agreement is reached by using our approach.
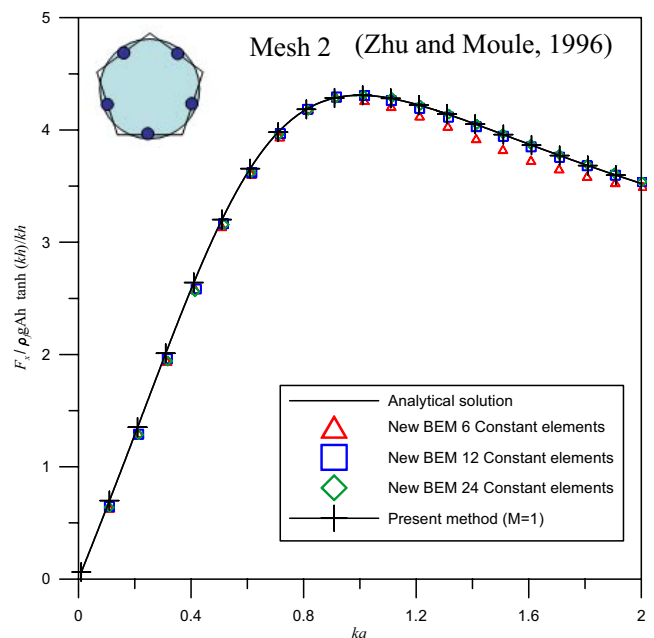

Fig. 5 Horizontal force on single cylinder using Mesh 2 of BEM and null-field BIEM
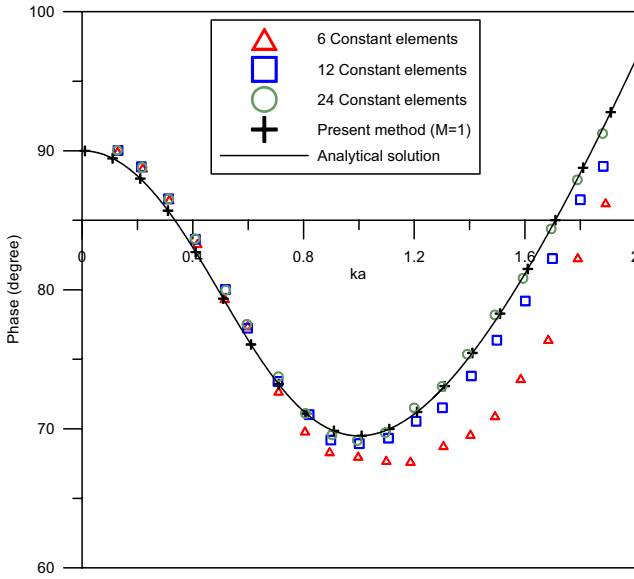
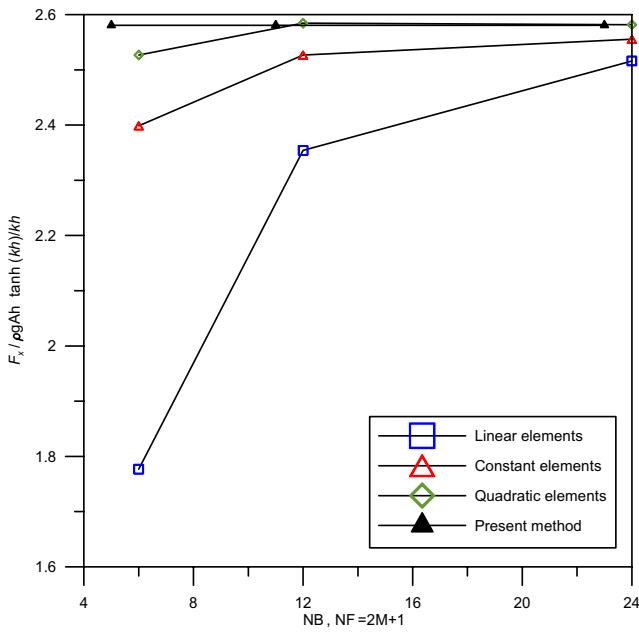Fig. 6 Phase of horizontal force on single vertical cylinder

Fig. 7 Convergence curve of horizontal force for single cylimder

The convergence rate of the horizontal force was also studied by Au and Brebbia (1983). Their results are also compared with those of BEM, using constant, linear and quadratic boundary elements as shown in the convergence curve of Fig. 7. It is amazing to find that the error obtained by using linear elements is larger

(a) 4 cylinders ($ka = 2.7657$)   (b) 9 cylinders ($ka = 2.7131$)

(c) 9 cylinders ($ka = 2.8252$)   (d) 9 cylinders ($ka = 2.7629$)
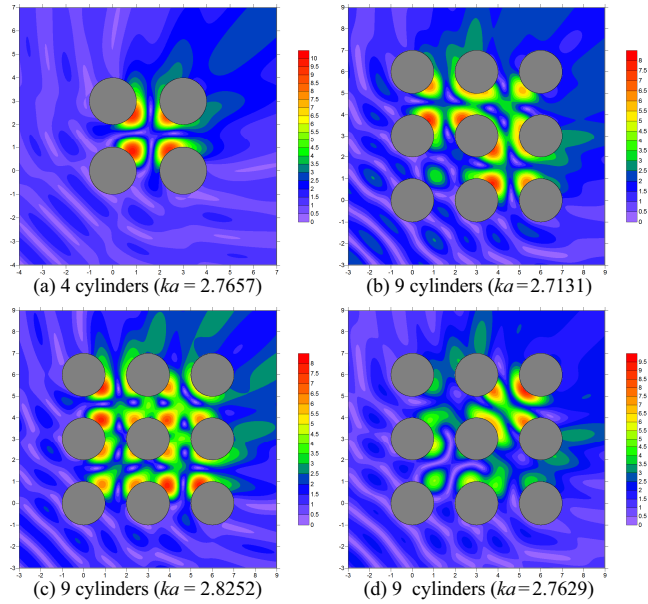
Fig. 8 Water wave elevation on near-trapped mode

than that obtained by using constant elements (Au and Brebbia, 1983). The possible reason is that the horizontal force is obtained by integrating the $\cos\theta$ term, which is an even function. It is a surprise that using only a few numbers of Fourier terms can obtain better accuracy than using 24 boundary elements.

Table 1 shows the better accuracy of the present method over the BEM. The incident angle is zero; the analytical solution of the horizontal force is 4.309. In addition, the results of the present method are more accurate than those of Zhu and Moule (1996), using a better mesh (Mesh 2) than Au and Brebbia (Mesh 1).

Case 2: Water Wave Impinging on 4 Circular Cylinders—Near-Trapped Mode

In Case 2, we consider the water wave structure problem by 4 and 9 bottom-mounted vertical rigid circular cylinders. The arrangements of 4 and 9 cylinders have radius 1 and the cylinder centers are spaced 3 apart (Fig. 8), and we focus on the physical phenomena of the near-trapped mode. Meylan and Taylor (2009) studied this problem in the complex plane of the water wave. Our program can detect the near-trapped mode by the direct-searching scheme for k in the real axis.

The scattering frequency of the near-trapped mode of the present method is compared with the Meylan and Taylor (2009) result. Fig. 9 shows the location of the scattering frequencies of the near-trapped mode in the complex plane for the 2 arrangements by Meylan and Taylor. Good agreement is reached. One

	Traditional discretization		New discretization		Present method $N_f = 2M+1$ ($ka = 1$)		
Elements	Force	Error (%)	Force	Error (%)		Force	Error (%)
$N_b = 6$	4.009	7	4.276	0.8	$P = 2$	4.309	2.26×10^{-15}
$N_b = 8$	4.141	4	4.294	0.3	$P = 3$	4.309	2.26×10^{-15}
$N_b = 12$	4.234	2	4.302	0.2	$P = 5$	4.309	2.26×10^{-15}
$N_b = 24$	4.29	0.4	4.307	0.04	$P = 11$	4.309	2.26×10^{-15}

N_b = Number of BEM elements and N_f is the number of the present method's Fourier series terms.

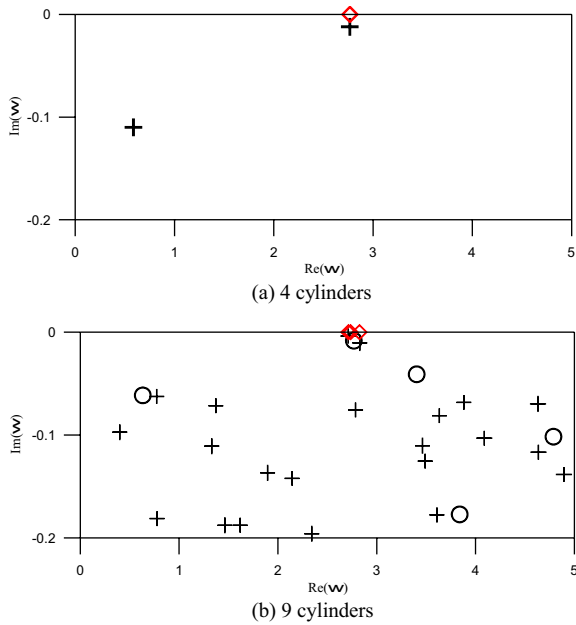Table 1   Computed forces and relative errors versus number of elements

(a) 4 cylinders

(b) 9 cylinders

Fig. 9 Locations of scattering frequencies of near-trapped mode in complex plane; single roots, +; double roots, ∘; present method = ◇

real scattering frequency close to the real axis for the 4 cylinders at 2.7641–0.0122i is found to be 2.7657 along the real axis by using our method. Regarding 9 cylinders, 3 real scattering frequencies close to the real axis for 9 cylinders at 2.7114–0.0041i (single root), 2.8284–0.0102i (single root) and 2.7635–0.0086i (double root) are found to be 2.7131, 2.8252 and 2.7629 on the real axis by using our method. Also shown in Fig. 8 are the water wave elevations on the near-trapped mode scattering frequencies;
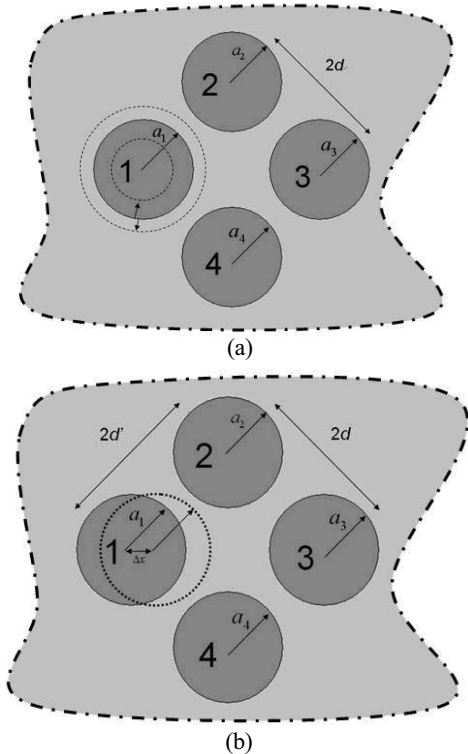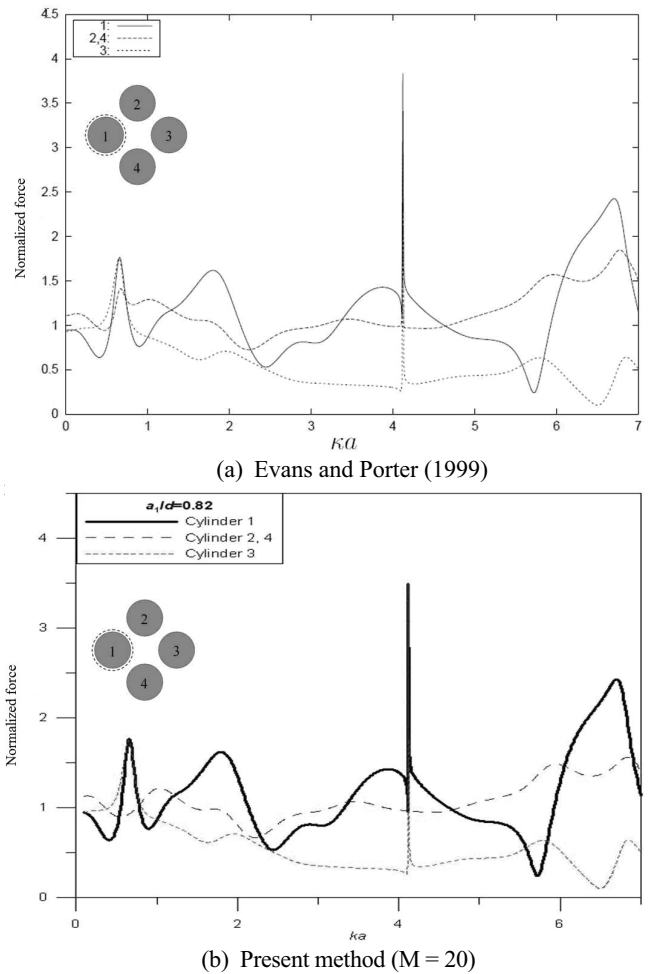

(a) Evans and Porter (1999)

(b) Present method (M = 20)

Fig. 11 Resultant force on unsysmmetric pattern of 4 cylinders against wave number, ka, ($\theta_{inc} = 0°$, $a_1/d = 0.82$, $a_i/d = 0.8$, $I = 2, 3, 4$) when radius expanded

we can find that the real parts of the complex poles near the real axis (Meylan and Taylor, 2009) are very close to ours. This confirms that our formulation and program can predict the near-trapped mode in the real axis free of the complicated computation in the complex k plane.

Case 3: Water Wave Impinging on 4 Circular Cylinders—Disorder of Periodical Pattern

In Case 3, the geometry and water wave condition are the same as in Case 2 except for the disorder of cylinder 1 and the cylin-

(a)

(b)

Fig. 10 Sketch of 4 cylinders: (a) expansion of radius for cylinder 1; (b) perturbation of center of cylinder 1

		Cylinder 1	Cylinder 3
a_1/d	$a_i/d\ i = 2, 3, 4$	Normalized force	Normalized force
0.86	0.8	1.15	0.25
0.84	0.8	1.20	0.25
0.82	0.8	1.30	0.27
0.80	**0.8**	**54.1**	**54.1**
0.78	0.8	1.02	0.34
0.76	0.8	1.13	0.30
0.74	0.8	1.19	0.30

Table 2 Resultant force generated by changing radius to destroy periodical setup ($ka = 4.08482$)

a_1/d'	$a_i/d \ i = 2, 3, 4$	Cylinder 1 Normalized force	Cylinder 3 Normalized force
0.86	0.8	1.15	0.29
0.84	0.8	1.20	0.28
0.82	0.8	1.27	0.27
0.80	**0.8**	**54.1**	**54.1**
0.78	0.8	1.12	0.27
0.76	0.8	1.17	0.26
0.74	0.8	1.16	0.26

Table 3   Resultant force generated by moving center of one cylinder to destroy periodical setup ($ka = 4.08482$)
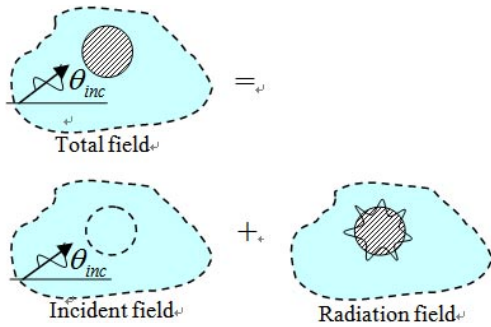

Fig. 12 Total field divided into 2 fields

der centers being spaced 2.5 apart. Two kinds of disorder can destroy the periodical pattern. One is to expand the radius of the first cylinder to be different from other cylinders, as shown in Fig. 10a. The second is to perturb the center of the first cylinder, as in Fig. 10b. After comparing with the Evans and Porter (1999) result, good agreement is reached, as shown in Figs. 11a, b. The parameter study for the disorder on the near-trapped mode of $ka = 4.08482$ is examined. Tables 2 and 3 indicate that the peak value for the near-trapped mode is reduced significantly due to the perturbation of the radius and displacement of the center of one cylinder, respectively.

ANIMATION OF FREE-SURFACE ELEVATION FOR WATER WAVE PROBLEM CONTAINING A CIRCULAR CYLINDER

We can divide the total field into 2 fields. One is the incident field without any cylinder; the other is the radiation field with no incident wave (Fig. 12). The incident wave potential can be easily obtained (Chen et al., 2009a). The radiation potential can be derived by using the present method. After combining the potential's 2 parts, we can obtain the total field. The total potential by using this approach is as follows:

$$u(\mathbf{x}) = J_0(k\rho) + 2\sum_{m=1}^{\infty} (i)^m J_m(k\rho)\cos(m\phi - m\theta_{inc})$$

$$+ \left\{ \frac{\pi k a i}{2} \sum_{m=0}^{\infty} (i)^m \varepsilon_m H_m^{(1)}(k\rho) J_m'(ka) \right.$$

$$\left. \cdot \left(J_m(ka) - \frac{H_m^{(1)}(ka) J_m'(ka)}{H_m'^{(1)}(ka)} \right) \cos(m\phi - m\theta_{inc}) \right\}. \quad (45)$$

Finally, the animation for the total free-surface elevation can be constructed by using the Mathematica software as shown in Fig. 13.

CONCLUSIONS

In this paper, we employed the null-field BIEM formulation by using degenerate kernels for solving water wave scattering problems containing circular cylinders. The null-field integral equation and the Fourier series are in conjunction with adap-

(a) $t = 0$ (b) $t = 0.3$ (c) $t = 0.6$

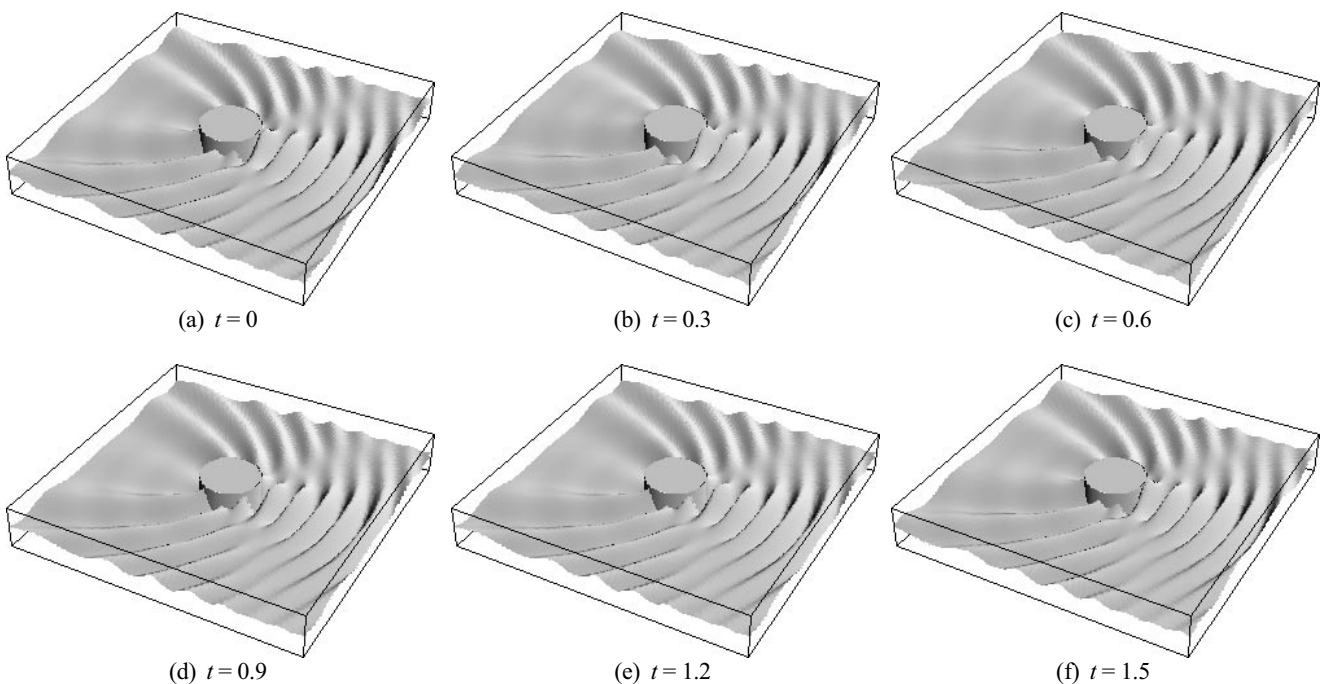(d) $t = 0.9$ (e) $t = 1.2$ (f) $t = 1.5$

Fig. 13 Animation of free-surface elevation for single circular cylinder

tive observer systems and vector decomposition. This method is a semi-analytical approach since only the truncation error in the Fourier series terms is involved. The results compare well with the results of Au and Brebbia (1983) and Zhu and Moule (1996) for a single cylinder. The convergence rate of the present method is faster than BEM's. Physical phenomena of the near-trapped mode for an array of cylinders were observed. The real wave numbers of scattering resonance for near-trapped modes are also compared with the complex poles of Meylan and Taylor (2009). Good agreements are reached near the real axis. By perturbing the radius of one cylinder ($a_1/d \neq 0.8$) or moving the center of one cylinder to destroy the periodical setup, the near-trapped mode can be suppressed obviously. The free-surface elevation and resultant forces on each cylinder have been presented to illustrate the effect of disorder of the periodical layout on suppressing the near-trapped modes. The results compare well with those of Evans and Porter (1999). Finally, the animation for the water wave containing a single cylinder using the Mathematica was given.

REFERENCES

Au, MC, and Brebbia, CA (1983). "Diffraction of Water Waves for Vertical Cylinders Using Boundary Elements," *Appl Math Modelling*, Vol 7, pp 106–114.

Chakrabarti, SK, and Tam, WA (1975). "Interaction of Waves with Large Vertical Cylinder," *J Ship Res*, Vol 19, pp 23–33.

Chen, JT, and Hong, HK (1999). "Review of Dual Boundary Element Methods with Emphasis on Hypersingular Integrals and Divergent Series," ASME, *Appl Mech Rev*, Vol 52, pp 17–33.

Chen, JT, Shen, WC, and Wu, AC (2006). "Null-Field Integral Equations for Stress Field Around Circular Holes Under Anti-Plane Shear," *Eng Analyt Bound Elem*, Vol 30, pp 205–217.

Chen, JT, and Lee, YT (2007a). "Interaction of Water Waves with an Array of Vertical Cylinders Using Null-Field Integral Equations," Presented at *14th Nat Computat Fluid Dynam Conf*, Nantou, Taiwan.

Chen, JT, Chen, CT, Chen, PY, and Chen, IL (2007b). "A Semi-Analytical Approach for Radiation and Scattering Problems with Circular Boundaries," *Computat Methods Appl Mech Eng*, Vol 196, pp 2751–2764.

Chen, JT, Chou, KS, and Kao, SK (2009a). "One-dimensional Wave Animation Using Mathematica," *Computat Appl Eng Educ*, Vol 17, pp 323–339.

Chen, JT, Lee, YT, and Lin, YJ (2009b). "Interaction of Water Waves with Arbitrary Vertical Cylinders Using Null-Field Integral Equations," *Appl Ocean Res*, Vol 31, pp 101–110.

Chen, IL, Wu, CF, Tsai, JJ, and Chen, JT (2009c). "Interaction of Water Waves with Vertical Cylinders Using Dual Boundary Element Method," Presented at *23rd Asian-Pacific Tech Exchange and Advisory Mtg on Marine Struct*, Kaohsiung, Taiwan.

Duclos, G, and Clément, AH (2004). "Wave Propagation Through Arrays of Unevenly Spaced Vertical Piles," *Ocean Eng*, Vol 31, pp 1655–1668.

Evans, DV, and Porter, R (1999). "Trapping and Near-Trapping by Arrays of Cylinders in Waves," *J Eng Math*, Vol 35, pp 149–179.

Graff, KF (1975). *Wave Motion in Elastic Solids*, Ohio State Univ Press, Columbus, Ohio, US.

Lee, JW, and Chen, JT (2010). "Null-Field Boundary Integral Equation Approach for Hydrodynamic Scattering by Multiple Circular and Elliptical Cylinders," Presented at *8th Asian Computat Fluid Dynam Conf*, Hong Kong.

Linton, CM, and Evans, DV (1990). "The Interaction of Waves with Arrays of Vertical Circular Cylinders," *J Fluid Mech*, Vol 215, pp 549–569.

MacCamy, RC, and Fuchs, RA (1954). "Wave Force on Piles: A Diffraction Theory," Coastal Eng Res Center, US Army, Tech Memo 69, Washington, DC.

Mei, CC (1983). *The Applied Dynamics of Ocean Surface Waves*, Wiley InterScience, Hoboken, New Jersey, US.

Meylan, MH, and Taylor, RE (2009). "Time-Dependent Water-Wave Scattering by Arrays of Cylinders and the Approximation of Near Trapping," *J Fluid Mech*, Vol 631, pp 103–125.

Postnova, J, and Craster, RV (2008). "Trapped Modes in Elastic Plates, Ocean and Quantum Waveguides," *Wave Motion*, Vol 45, pp 565–579.

Tabaei, A, and Mei, CC (2009). "Viscous Effects on Bragg Scattering of Water Waves by an Array of Piles," *Physical Rev E*, Vol 79, pp 026314-1–026341-14.

Wu, CF, Lin, YJ, Chen, IL, and Chen, JT (2009). "Study of Near-Trapped Modes and Fictitious Frequencies Using Null-Field Integral Equations," Presented at *33rd Nat Conf on Theoret and Appl Mech*, Miaoli, Taiwan.

Zhu, S, and Moule, G (1996). "An Efficient Numerical Calculation of Wave Loads on an Array of Vertical Cylinders," *Appl Math Modelling*, Vol 20, pp 26–33.